Remediation of liquefaction effects for an embankment using soil-cement walls: Centrifuge and numerical modeling

Ross W. Boulanger[a,*], Mohammad Khosravi[a], Ali Khosravi[a], Daniel W. Wilson[b]

[a] Department of Civil and Environmental Engineering, University of California, Davis, CA 95616, USA
[b] Center for Geotechnical Modeling, University of California, Davis, CA 95616, USA

A B S T R A C T

Numerical simulations of a centrifuge model test of an embankment on a liquefiable foundation layer treated with soil-cement walls are presented. The centrifuge model was tested on a 9-m radius centrifuge and corresponded to a 28 m tall embankment underlain by a 9 m thick saturated loose sand layer. Soil-cement walls were constructed through the loose sand layer over a 30 m long section near the toe of the embankment and covered with a 7.5 m tall berm. The model was shaken with a scaled earthquake motion having peak horizontal base accelerations of 0.05 g, 0.26 g, and 0.54 g in the first, second, and third events, respectively. The latter two shaking events caused liquefaction in the loose sand layer. Crack detectors embedded in the soil-cement walls showed that they developed only minor cracks in the second shaking event, but sheared through their full length in the last shaking event. The results of the centrifuge model test and two-dimensional nonlinear dynamic simulations are compared for the two stronger shaking events using procedures common in engineering practice. The effects of various input parameters and approximations on simulation results are examined. Capabilities and limitations in the two-dimensional simulations of soil-cement wall reinforcement systems, with both liquefaction and soil-cement cracking effects, are discussed. Implications for practice are discussed.

1. Introduction

Soil-cement grid and wall systems have been used to remediate embankment dams and other civil infrastructure against the effects of earthquake-induced liquefaction in their foundations. Soil-cement treatments have the advantage that they can be constructed in a wide range of soils, including silty soils that can be difficult to treat by densification techniques. A soil-cement grid or wall system is often constructed near the toe of an embankment and covered with an overlying berm to increase confinement and reduce deformations that bypass the treatment zone. An example of this type of configuration is the remediation at the 24-m tall Clemson Upper and Lower Diversion Dams (Wooten and Foreman [23]) as shown in Fig. 1. Other embankment dam remediation projects using soil-cement grid or wall systems in the US include: Sunset North Basin Dam, CA (about 23 m high; Barron et al. [2]); San Pablo Dam, CA (about 44 m high; Kirby et al. [14]); Perris Dam, CA (about 39 m high; Friesen and Balakrishnan [9]), and Chabot Dam, CA (about 30 m high; EBMUD).

The seismic performance of soil-cement grids and walls have been studied using three-dimensional (3D) analysis methods (e.g., Fukutake and Ohtsuki [10], Namikawa et al. [16]), but design practices generally rely on two-dimensional (2D) approximations with equivalent composite strengths for the treatment zones (e.g. Wooten and Foreman [23], Barron et al. [2], Kirby et al. [14], Friesen and Balakrishnan [9]). Some

common concerns in the design of soil-cement grids for liquefaction remediation include the potential for cracking and brittle failure in the soil-cement elements, the ability of 2D analysis procedures to approximate the 3D response, and the lack of experimental or case history data to validate 2D or 3D numerical analysis methods.

This paper presents results of centrifuge model tests and numerical simulations of an embankment on a liquefiable foundation layer treated with soil-cement walls, expanding on results presented in Boulanger et al. [4]. The centrifuge model was tested on a 9-m radius centrifuge and corresponded to a 28 m tall embankment underlain by a 9 m thick saturated loose sand layer (prototype units). Soil-cement grids were positioned through the loose sand layer near the toe of the embankment and covered with a berm. The model was shaken three times with a scaled earthquake motion; the peak horizontal base accelerations (PBA) were 0.05 g, 0.26 g and 0.54 g, respectively. The latter two events liquefied the loose sand layer. The soil-cement walls developed limited cracking in the 0.26 g shaking event and sheared through their full length in the 0.54 g event. Two-dimensional nonlinear dynamic analyses were performed using the finite difference program FLAC (Itasca [11]) and the user-defined constitutive model PM4Sand (Boulanger and Ziotopoulou [6]) for the sands. The treatment zone was represented with area-averaged composite properties as is common in design practice. The centrifuge model test and numerical simulation procedures are described, followed by comparisons of the measured and

---
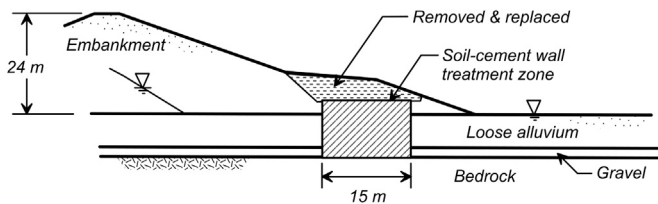
Fig. 1. Soil-cement shear walls at Clemson Diversion Dams, SC (after Wooten and Foreman [23]).

simulated responses. The effects of various input parameters and approximations on simulation results are examined. Capabilities and limitations in the two-dimensional simulations of soil-cement wall reinforcement systems, with both liquefaction and soil-cement cracking effects, are discussed. Implications of the centrifuge and numerical analysis results for practice are discussed.

2. Centrifuge model tests

The centrifuge model was tested in a flexible shear beam container at a centrifugal acceleration of 65 g on the UC Davis 9-m radius centrifuge. Standard scaling laws are followed and results are presented in prototype units unless otherwise specified. The experiment and data are documented for distribution in Khosravi et al. [12] and summarized in Khosravi et al. [13].

The centrifuge model configuration (Fig. 2) consisted of a foundation
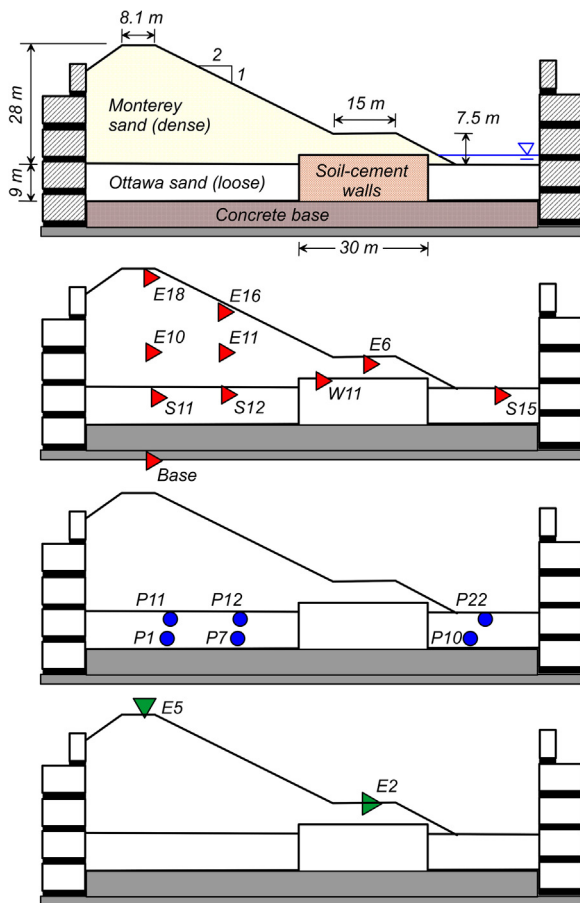
Fig. 2. Cross-sections showing model dimensions (prototype scale) and the locations of accelerometers (red triangles), pore pressure transducers (blue circles), and displacement transducers (green triangles) that are later compared with simulation results. (For interpretation of the references to color in this figure legend, the reader is referred to the web version of this article.)

layer of loose Ottawa F-65 sand (relative density, D_r = 42%; D10 = 13 mm), an embankment and berm of dry, dense Monterey #0/30 sand (D_r = 85%; D10 = 0.4 mm), and a set of nine parallel soil-cement panels over a 30 m long section near the toe of the embankment. The pore fluid was a methylcellulose solution with a viscosity about 15 times that of water. The water table was above the top of the foundation layer and slightly above the tops of the walls. A thin layer of Monterey medium aquarium sand (D_{10} = 1.7 mm) was placed at the water surface elevation to provide a capillary break during model construction.

The soil-cement walls were formed and cured in molds and then arranged in the flexible shear beam container prior to pluviation of the foundation sand layer. The walls were 1.4 m thick and spaced 5.8 m apart (center to center), for an area replacement ratio of A_r = 24%. The soil-cement had an average unconfined compressive strength (q_{ucs}) of 2.06 MPa at the time of centrifuge testing. The walls were set into preformed slots in a concrete base layer and grouted into position.

Seventeen crack detectors were embedded in four of the soil-cement walls at the time they were formed. The crack detectors were 2-mm diameter pencil leads connected to a circuit by wires at each end (Tamura et al. [20]). These brittle conductors provide a binary indication of if, and when, cracking occurs. The pencil leads were oriented vertically at different locations along the walls, with their lower end below the top of the concrete base.

The model was also extensively instrumented with accelerometers, pore pressure transducers, and displacement transducers as described in Khosravi et al. [13]. The locations of the transducers whose recordings are later compared with simulation results are shown on the cross-sections in Fig. 2.

The model was shaken three times with a scaled version of a recording from Port Island in the 1995 Kobe earthquake. The first shaking event had a PBA = 0.05 g, for which the response was essentially elastic with no excess pore pressure generated. The second shaking event had a PBA = 0.26 g, which triggered liquefaction in the saturated sand layer but caused only minor cracking in the soil-cement walls. The third shaking event was applied long after full dissipation of the excess pore pressures from the second event; it had a PBA = 0.54 g, triggered liquefaction throughout the saturated sand layer, and caused the soil-cement walls to develop shears/cracks through their full lengths. The crest settled about 0.7 m and the toe berm displaced laterally about 1.3 m in the PBA = 0.54 g event, whereas movements in the PBA = 0.26 g event were only a quarter to half these amounts.

A photograph of the soil-cement walls when the foundation soils had been excavated to the elevation of a blue paper marker is shown in Fig. 3. The blue markers were placed flush against the faces of the soil-cement walls on the upstream and downstream faces during construction. The blue markers have been pushed forward between the soil-cement walls on the upstream side (by approximately 0.1 m), and pushed away from the walls by up to 0.8 m on the downstream side. These photos illustrate how the loose sand between the walls, which liquefied during strong shaking, displaced downslope relative to the walls during the course of imposed shaking.

Photographs of the soil-cement walls during model dissection after testing are shown in Fig. 4. Crack detectors indicate that only portions of the panels were cracked during the PBA = 0.26 g event, such that the majority of damage and the offsets along the cracks occurred during the larger PBA = 0.54 g shaking event.

3. Numerical simulation model

Two-dimensional (2D) nonlinear dynamic analyses were performed using the finite difference program FLAC (Itasca [11]). The mesh and material zones are shown in Fig. 5. Analyses were performed in large-strain mode with coupled pore water flow. Analyses used 0.5% Rayleigh damping at a frequency of 1 Hz.

The sands were modeled using the user-defined constitutive model PM4Sand version 3, which is a stress-ratio controlled, critical state
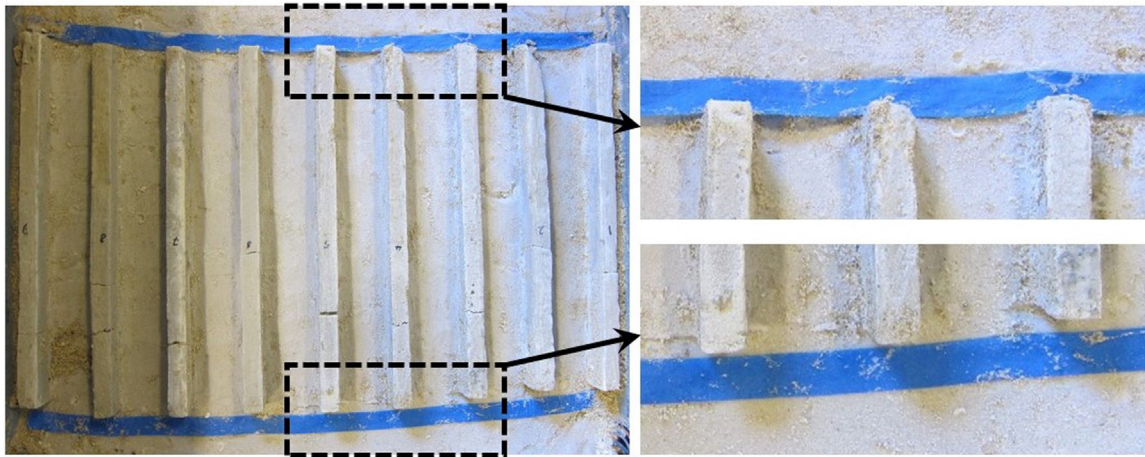
Fig. 3. Post-test excavation with exposed paper markers (originally aligned in contact with panels) showing the liquefied sand moved slightly more than the soil-cement panels on the embankment side (top of photo; note the bowing of the marker between panels) and significantly more than the panels on the toe side (bottom of photo; note the gaps between the panels and the marker). It is also evident that the panels in the middle moved downstream (toward the bottom) more than panels near the container boundaries.

Fig. 4. Post-test excavation photos of the soil-cement panels (toe of berm is to left side of photos).

compatible, bounding surface plasticity model developed for earthquake engineering applications (Boulanger and Ziotopoulou [5,6], Ziotopoulou and Boulanger [26]). This constitutive model requires specification of three primary input parameters, all of which are dimensionless: apparent relative density, D_r; shear modulus coefficient, G_o; and contraction rate parameter, h_{po}. The optional secondary parameters receive default values per the calibration described by Ziotopoulou and Boulanger [25] if the user does not specify them. The dynamic link library and example files for this model for use with FLAC is available for download at https://pm4sand.engr.ucdavis.edu/.

The parameters for the loose sand layer were obtained by calibration against results of cyclic direct simple shear tests on Ottawa F-65 sand by Parra Bastidas et al. [18,19], which included the effects of prior cyclic loading history. The cyclic stress ratio (CSR) to cause a peak shear strain of 3% (or an excess pore pressure ratio of 100%) in 15 uniform loading cycles at a vertical effective consolidation stress (σ'_{vc}) of 400 kPa was 0.093 for virgin specimens (i.e. applicable for the PBA = 0.05 g and 0.26 g shaking events) and 0.120 after one liquefaction event (i.e. applicable for the PBA = 0.54 g shaking event). The D_r was estimated to increase from 42% for the virgin model to 45% after one liquefaction event based an estimated reconsolidation strain of 0.6%. The small-strain shear modulus parameter, G_0, was determined from a correlation for Ottawa sand as reported in Parra Bastidas [18]. Two secondary parameters were assigned values based on the available index test data for Ottawa F-65 sand: maximum void ratio $e_{max} = 0.83$ and minimum void ratio $e_{min} = 0.51$. Lastly, the h_{po} parameter was
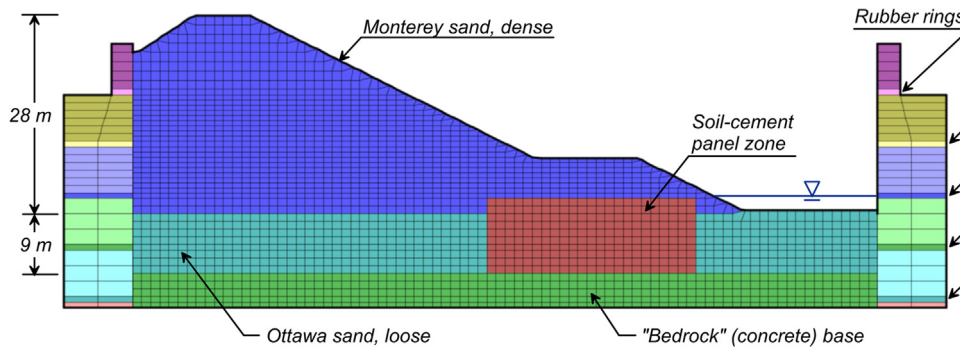
Fig. 5. Two-dimensional mesh and material zones.
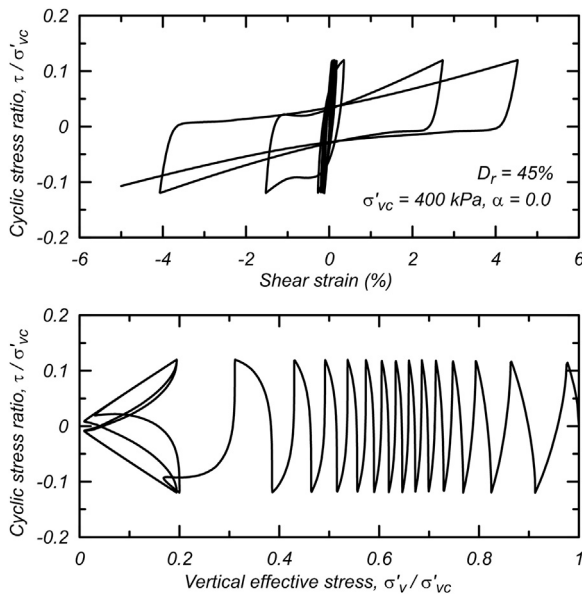
Fig. 6. Response of calibrated PM4Sand model in cyclic undrained simple shear loading with zero initial static shear stress.

determined by successive iterations until the cyclic direct simple shear strengths from single-element simulations agreed with the above target strengths. The calibrated parameters for these analyses are D_r = 42%, G_o = 770, and h_{po} = 0.54 for the PBA = 0.26 g event, and D_r = 45%, G_o = 788, and h_{po} = 1.20 for the PBA = 0.54 g event. The response of the constitutive model with the calibration for the second event is illustrated in Fig. 6 showing the stress-strain and stress path responses to undrained, uniform cyclic, direct simple shear loading with an initial static shear stress ratio ($\alpha = \tau_{hv}/\sigma'_{vo}$) of zero.

The undrained cyclic loading response of the calibrated model with a nonzero static shear stress bias is important for these analyses of sloping ground conditions. The response of PM4Sand under sloping ground conditions with irregular cyclic loading is described in
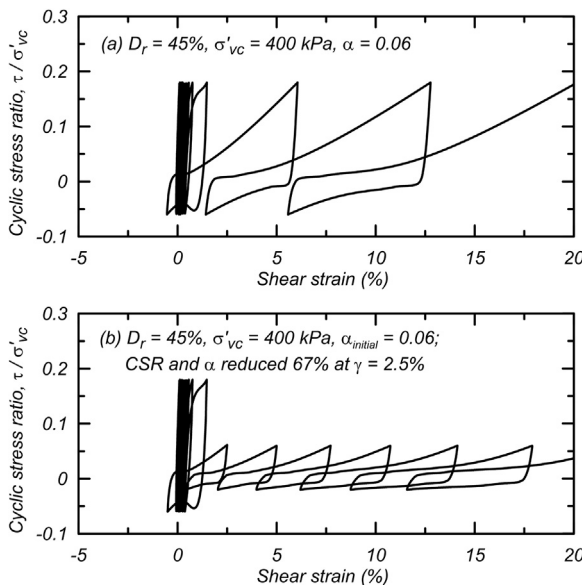
Fig. 7. Response of calibrated PM4Sand model in cyclic undrained simple shear loading with an initial static shear stress ratio of $\alpha = 0.06$: (a) with a uniform applied CSR, and (b) with the CSR and α reduced 67% once the peak shear strain reached 2.5%.

Ziotopoulou and Boulanger [26], and illustrated by two examples in Fig. 7 that are intended to approximate the loading conditions that will develop under the embankment. The response in Fig. 7a shows the stress-strain response for the same loading conditions as previously shown in Fig. 6, except with α = 0.06 instead of zero. The presence of the static shear stress bias causes shear strains to accumulate rapidly in the direction of the shear stress bias, as expected. The response in Fig. 7b shows the same loading again, except that the CSR and α are both reduced by 67% once the shear strain has exceeded 2.5%. This example illustrates how a drop in imposed loading during seismic loading slows the rate of shear strain accumulation. These single-element loading responses can later be qualitatively compared to the stress-strain responses obtained for points within the system model, as one additional basis for evaluating the consistency of the material and system responses.

The parameters for the dense coarse Monterey sand were similar to those used by Armstrong and Boulanger [1]. The three primary parameters were D_r = 85%, G_o = 1427, and h_{po} = 1.9. The secondary parameters assigned non-default values were e_{max} = 0.84, e_{min} = 0.54, and n^b = 0.6. The bounding surface parameter n^b was increased from 0.5 (default value) to 0.6 to increase peak effective friction angles by a couple degrees, thereby being in better agreement with peak friction angles predicted for this dense sand by Bolton's [3] relationship.

The soil-cement treatment zone was modeled using a Mohr Coulomb ($c − \phi$) model with area-weighted cohesion and friction angle properties. The soil-cement's average undrained shear strength during strong shaking was taken as 80% of the peak undrained shear strength, or $(S_u)_{wall} = 0.8(q_{ucs}/2) = 0.82$ MPa, to allow for some strain softening as the walls deform. This average resistance is intended to account for the actual shear resistance being closer to peak strength early in shaking and more than 20% below peak strength late in shaking. The saturated loose sand layer was assumed to contribute zero shear resistance to the composite system because its stress-strain response would be much softer than that of the soil-cement walls after it liquefies. Thus, the equivalent composite shear strength for the treatment zone in the loose sand layer was taken as $c = A_r \cdot (S_u)_{wall} = 0.198$ MPa with $\phi = 0$ for the 2D numerical analyses. The dense Monterey sand is assumed to contribute shear resistance to the composite system because it is not expected to liquefy during shaking. Thus, the equivalent composite shear strength for the treatment zone in the dense Monterey sand was taken as $c = 0.198$ MPa with $\phi = 32$ degrees. The equivalent composite tensile strength was set large for the baseline case, with the effect of tensile yielding evaluated later in parametric analyses. The elastic modulus of the soil-cement (E_{sc}) was taken as 300 q_{ucs} (618 MPa) (Bruce et al. [7]), while the bulk modulus (K_{sc}) was taken as 400 q_{ucs} (824 MPa) based on an estimated Poisson ratio of 0.2. The equivalent composite elastic and bulk moduli of the treatment zone were taken as $A_r \cdot E_{sc}$ and $A_r \cdot K_{sc}$, respectively.

The flexible shear beam container and the concrete base inside the container were modeled using linear elastic materials. The key physical characteristics of the container, including the metal and rubber rings, are listed in Table 1. The secant shear modulus for the current rubber in the container was determined from shear load tests on the container after it was rehabilitated in 2015, and the modulus reported in Table 1 represents the average apparent modulus across the entire container. The density and elastic moduli for each container element in the 2D numerical model (Fig. 5) were based on the mass and lateral stiffness properties of the container divided by the inside width of the container ($W_{container}$) (i.e., proportioning mass and stiffness per unit width of the enclosed soil). For example, the rubber below ring number 3 has a physical plan area (A_{rubber}) of 0.537 m² and shear modulus (G_{rubber}) of 0.8 MPa (Table 1), whereas the 2D numerical model has a plan area ($A_{rubber,2D}$) of only 0.3048 m²/m at model scale (i.e., the width of rubber under the ring on both sides of the 2D model). The equivalent shear modulus for the rubber in the 2D numerical model ($G_{rubber,2D}$) can then be computed at model scale as:

Table 1
Properties for flexible shear beam container FSB2.

Ring number	Material	Section: width by height (mm)	Mass of ring (kg)	Area of rubber on lower face (m^2)	Mass of rubber on lower face (kg)
1 (top)	Aluminum	Channel: 50.8 by 101.6	13.2	0.258	3.7
2	Aluminum	Tubing: 152.4 × 101.6	47.5	0.537	7.7
3	Aluminum	Tubing: 152.4 × 101.6	47.5	0.537	7.7
4	Aluminum	Tubing: 152.4 × 101.6	90.0	0.637	9.1
5 (bottom)	Steel	Tubing: 101.6 × 101.6 and 152.4 × 101.6	113.0	0.637	9.1

Note: Inside width of container, $W_{container}$ = 0.787 m; Shear modulus of rubber, G_{rubber} = 0.8 MPa; Thickness of rubber rings, H_{rubber} = 12.7 mm.

$$G_{rubber,2D} = \frac{G_{rubber} A_{rubber}}{W_{container} A_{rubber,2D}} \qquad (1)$$

The equivalent density of the rubber in the 2D numerical model ($\rho_{rubber,2D}$) can also be computed at model scale as:

$$\rho_{rubber,2D} = \frac{\rho_{rubber} V_{rubber}}{W_{container} V_{rubber,2D}} = \frac{M_{rubber}}{W_{container} V_{rubber,2D}}, \qquad (2)$$

where the physical mass of the rubber (M_{rubber}) in this example is 7.7 kg and the volume of the rubber in the 2D numerical model ($V_{rubber,2D}$) is 0.00387 m^3/m (i.e., the rubber's plan area times its thickness of 12.7 mm). The above values for $G_{rubber,2D}$ and $\rho_{rubber,2D}$ are applicable for the prototype scale 2D numerical model since these parameters scale by unity. The above approach was repeated for each ring and rubber layer.

The foundation and embankment sands were connected to the container rings by interface elements. The end walls of the flexible shear beam container include rough vertical elements to carry complimentary shear stresses (Wilson et al. [22]), so the numerical interface elements were assigned a friction angle of 40 degrees and a nominal cohesion of 5 kPa. The interfaces were generally stronger than the adjacent sands, which effectively limited the amount of slip that developed along these interfaces. Sensitivity analyses showed that reducing the interface strength within a reasonable range did not significantly affect the global response of the model.

Hydraulic conductivities (k) were assumed isotropic for both soils and the treatment zone. The loose Ottawa sand layer was assigned k = 0.0192 cm/s based on laboratory tests data summarized in Parra Bastidas et al. [17]. The dense Monterey sand was assigned a k ten times that of the Ottawa sand where it was saturated (based on their grain size differences) and one tenth that of the Ottawa sand where it was unsaturated. The effect of partial saturation on k was estimated using published data and generalized relationships (e.g. Zhang and Fredlund [24]). The soil-cement treatment zone was assigned area-weighted values of porosity and hydraulic conductivity. The free water at the toe was modeled as a boundary pressure.

4. Initial stress conditions

The initial static stress conditions for the numerical model were established using gravity turn-on with the simpler Mohr-Coulomb model used for all materials. The shear moduli for all sand materials were taken as confinement dependent, with the shear moduli computed based on estimated values for mean effective stress at each depth. The friction angle for the Ottawa sand was taken as 32 degrees, whereas the friction angle for the Monterey sand was reduced to 22 degrees (based

on a sensitivity study) to indirectly ensure that initial lateral earth pressure conditions were reasonable (as discussed later) and no unusual stress concentrations occurred throughout the model. A nominal cohesion of 2 kPa was also assigned to both sands. This approach does not reproduce the complex loading history associated with centrifuge model construction at 1 g followed by spin-up, but the explicit modeling of those steps would not necessarily produce improved results. Instead, the intent was to produce initial static stress conditions that are reasonable and consistent with expected patterns. After the initial stresses were initialized, the constitutive models for the sands were switched to PM4Sand and equilibrium solved for again.

The initial static stress conditions prior to dynamic loading are described in Fig. 8 in terms of the vertical effective stress (σ'_{vo}), the coefficient of lateral earth pressure (K_o), and the initial static shear stress ratio on horizontal planes (α). The contours of σ'_{vo} are smooth and approximately parallel to the ground surface. The values of K_o are between 0.4 and 0.5 throughout most of the embankment and foundation, but are as large as 1.5–2.5 at shallow depths along portions of the embankment face, the toe berm, and the foundation area between the berm and container wall. The values of $\alpha = \tau_{vh}/\sigma'_{vo}$ are between 0.0 and 0.3 for most of the body of the embankment and foundation, with higher values near the face of the embankment and berm slopes. The greater height of soil against the left side of the container causes the container to deform leftward (in both the physical and numerical models); this causes an increase in the lateral stresses (both normal and shear) in the foundation soil against the right side of the container, and it causes small variations in stress conditions near each rubber ring on the left side of the container (Fig. 5).

5. Dynamic simulation results

Numerical simulations were compared to measured responses for the PBA = 0.26 g and 0.54 g shaking events in terms of the accelerations, pore pressures, displacements, deformation patterns, and soil-cement damage patterns. Results for the PBA = 0.54 g event using the baseline set of input parameters, as described above, are presented to illustrate these comparisons.

5.1. Kobe event with PBA = 0.26 g

Simulated and measured accelerations for the PBA = 0.26 g event are compared in Fig. 9 for several points in the embankment, toe berm, foundation layer, and base (locations shown in Fig. 2). The linear elastic response spectra (5% damped) for these same motions are shown in Fig. 10. The amplitudes of the simulated acceleration time series are in reasonable agreement with the recorded accelerations throughout the embankment and foundation, although the simulations do have stronger high-frequency components for points within the liquefying foundation layer, on the embankment face, and at the surface of the toe berm (as evident in the spectra in Fig. 10).

Simulated and measured pore pressures for several points in the loose sand layer (locations shown in Fig. 2) are compared in Fig. 11. The measured excess pore pressures are far greater under the embankment (left two columns in Fig. 11) than in the free field beyond the toe (right column in Fig. 11), reflecting the differences in overburden stresses at these points. The pore pressures rise to values nearly equal to the estimated initial overburden stresses at these points, indicating that excess pore pressure ratios of, or near, 100% were triggered throughout the loose sand layer. The simulations reasonably track the rise in excess pore pressures, their peak values, and their dissipation rates after the end of strong shaking.

Simulated and measured displacements for the crest and berm are shown in Fig. 12. The measured displacements are from displacement transducers mounted on racks positioned across the top ring of the container, which moves horizontally relative to the container base during dynamic shaking. The simulation results for the horizontal
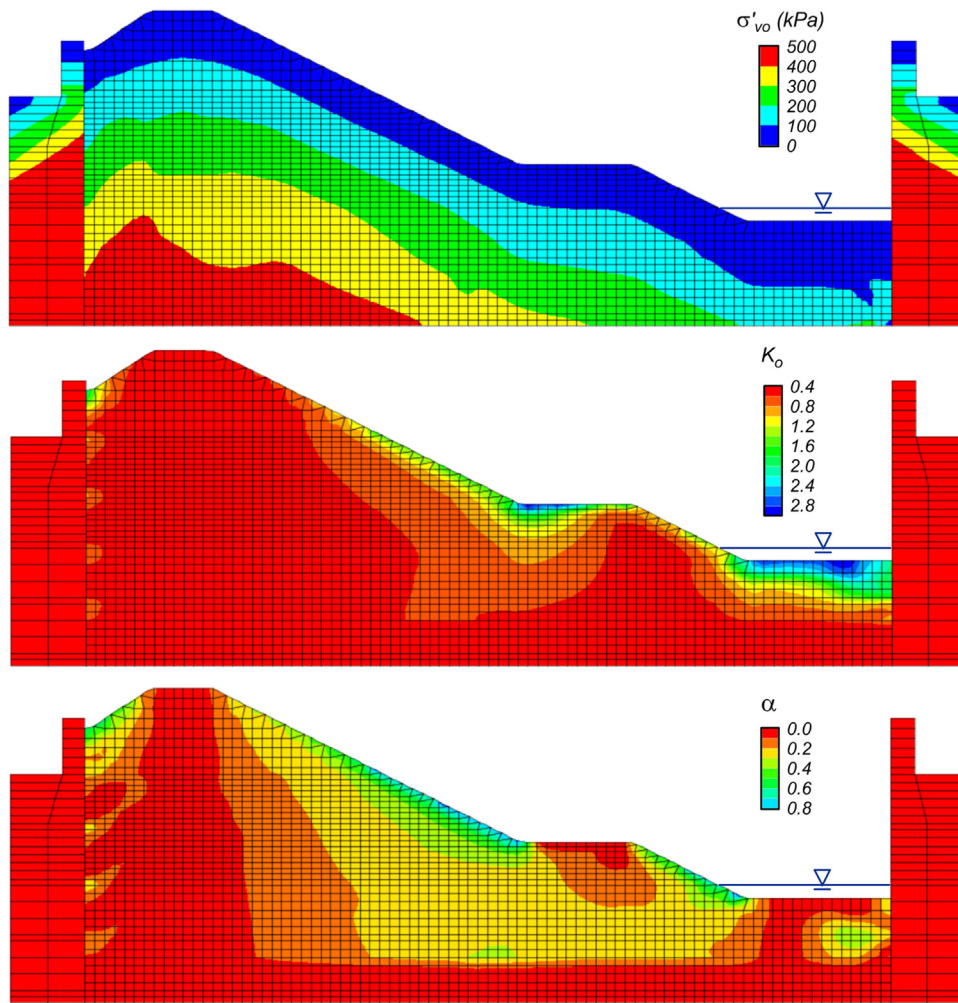
Fig. 8. Initial static stress conditions: vertical effective stress, coefficient of lateral earth pressure at rest, and initial static shear stress ratio on horizontal planes.
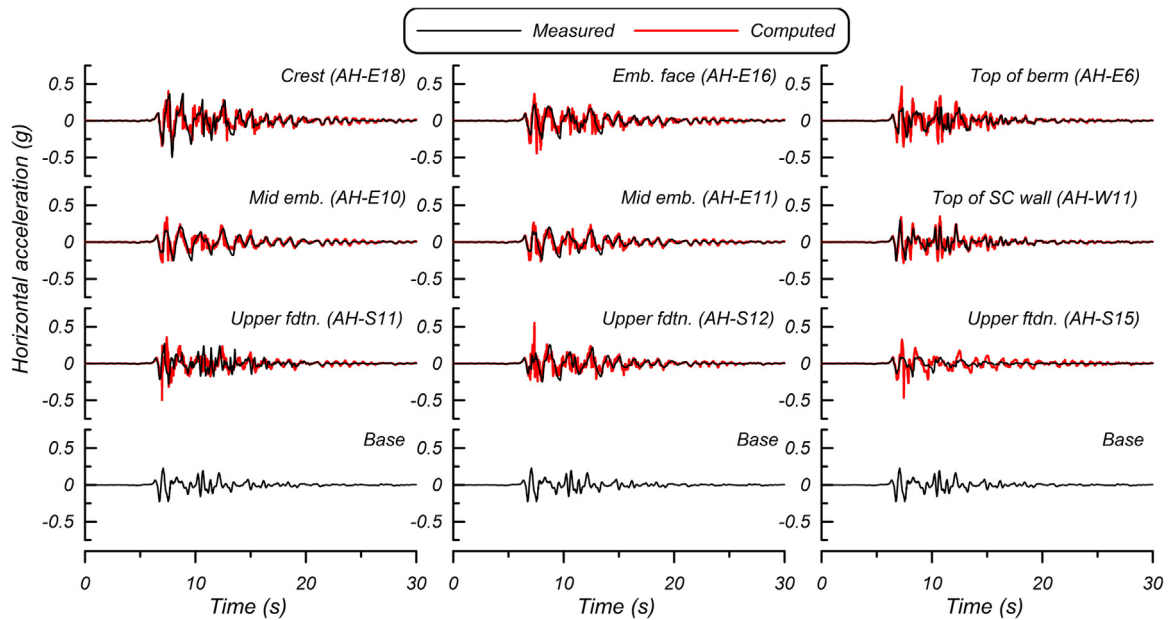
Fig. 9. Measured and computed accelerations for the Kobe 0.26 g event.
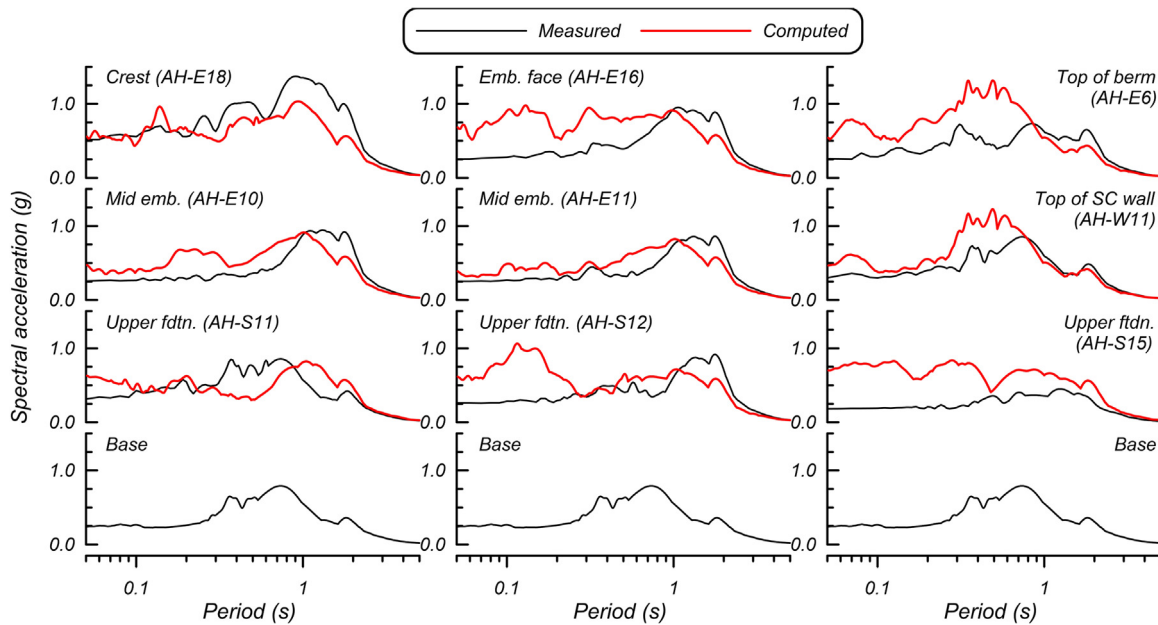
Fig. 10. Measured and computed accelerations for the Kobe 0.26 g event.

displacements are therefore also presented as relative to the top container ring. The simulations are in close agreement with the measured displacements throughout the course of shaking, including the dynamic component of the horizontal displacements.

The deformed mesh with contours of maximum (engineering) shear strain for the end of shaking is shown in Fig. 13. Note that FLAC reports the radius of the Mohr circle of strain, such that the values shown in this figure are twice those reported by FLAC. The computed deformation patterns and magnitudes are in reasonable agreement with those measured during testing. The simulation predicts that the soil-cement panels would develop engineering shear strains of up to about 8% near the base, even though the crack detectors showed cracking in only limited locations during this event.

The computed stress-strain response for a point in the loose Ottawa sand layer below the embankment crest (at the location of pore pressure transducer P1, Fig. 2) is shown in Fig. 14a. This figure shows the shear stress ratio on the horizontal plane (i.e. τ_{hv}/σ'_{vo}) versus the corresponding shear strain, γ_{hv}. The actual loading condition is more complex than pure simple shear, but this point is located in an area dominated by simple-shear deformations so examining the response along a horizontal plane is reasonable. The computed stress-strain response shows the loss of soil stiffness in the first couple of cycles as pore pressures rose rapidly, followed by a progressive accumulation of shear strains with each cycle of loading. The computed responses in this layer are consistent with the behaviors expected based on the single-element simulations performed during the constitutive model calibration process (e.g. Figs. 6 and 7, and Ziotopoulou and Boulanger [26]).
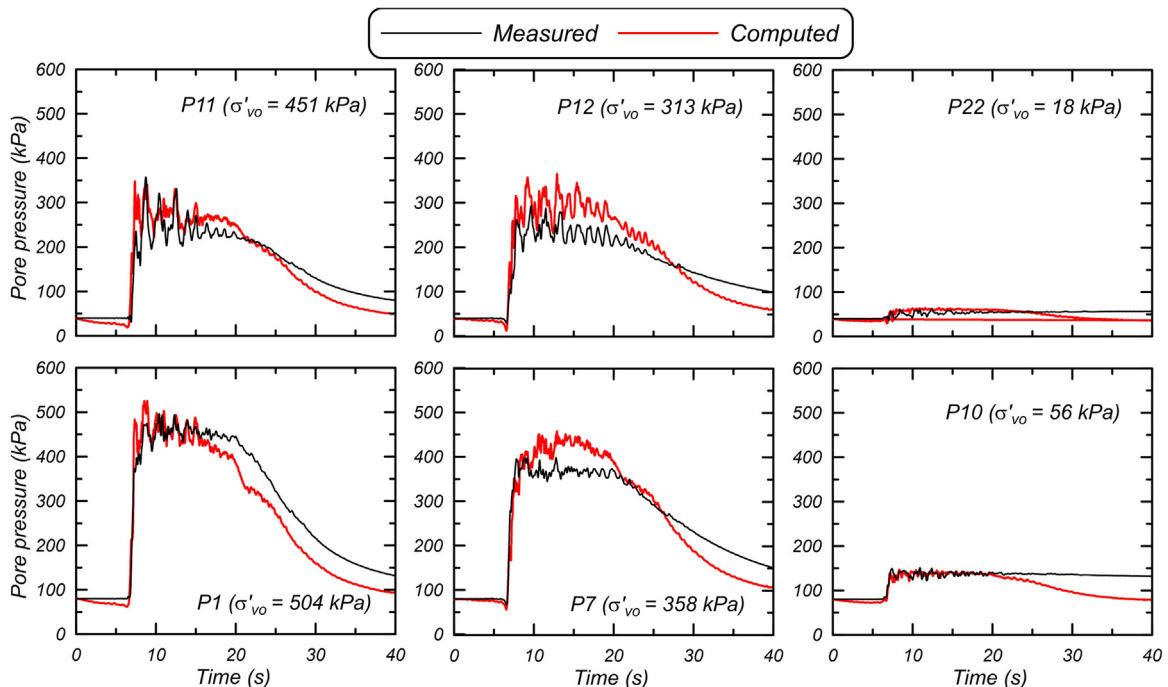
Fig. 11. Measured and computed excess pore water pressures for the Kobe 0.26 g event.
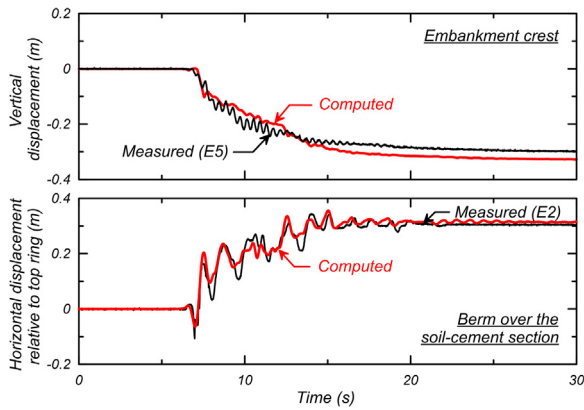
Fig. 12. Measured and computed crest settlement and berm horizontal displacement for the Kobe 0.26 g event.

5.2. Kobe event with PBA = 0.54 g

Simulated and measured accelerations for the PBA = 0.54 g event are compared in Fig. 15 for several points in the embankment, toe berm, foundation layer, and base. The linear elastic response spectra (5% damped) for these same motions are shown in Fig. 16. The measured accelerations in the loose sand layer exhibit large high frequency spikes that are associated with the cyclic mobility behaviors under this stronger level of shaking; the computed responses capture this cyclic mobility response but underestimate the magnitude of the acceleration spikes, as evident in both the accelerations (Fig. 15) and response spectra (Fig. 16). The simulations are otherwise in reasonable agreement with the recordings throughout the embankment and foundation.

Simulated and measured pore pressures for several points in the loose sand layer are compared in Fig. 17. The simulations reasonably track the rise in excess pore pressures, their peak values, and their dissipation rates after the end of strong shaking.

Simulated and measured displacements for the crest and berm, relative to the top container ring, are shown in Fig. 18. The computed horizontal displacement of the berm is in good agreement with the measured displacement throughout shaking, whereas the compute crest settlement is about 80% greater than the measured displacements.

The deformed mesh with contours of shear strain for the end of shaking with the PBA = 0.54 g event are shown in Fig. 19. The simulation predicts that the soil-cement panels would develop engineering shear strains of up to about 30% near their base, which is consistent with the observation that they shear through during this event (Fig. 4). The simulations also predict that the shear strains in the walls would be concentrated along their connection with the concrete base layer, whereas the post-testing photographs in Fig. 4 show that the cracks start at about ¼ to ½ the wall height on the upslope end, are closer to the bottom of the walls at the downslope end, and had irregular wavy surfaces that varied between walls.
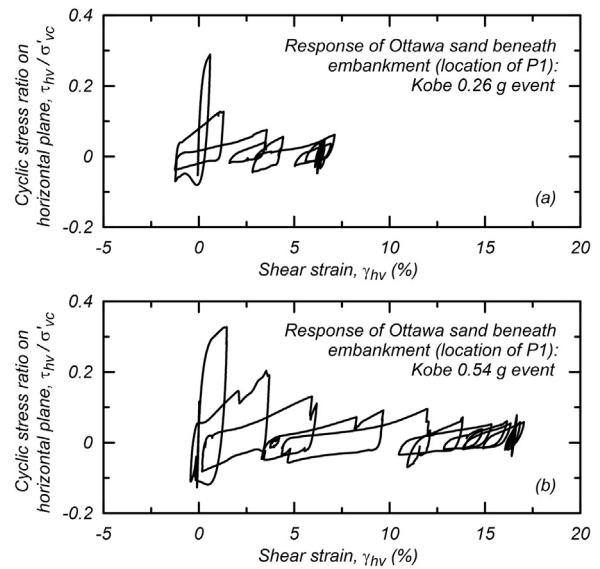
Fig. 14. Stress-strain response for a point in the loose Ottawa layer beneath the embankment crest (location of P1) during: (a) Kobe 0.26 g and (b) Kobe 0.54 g events.

The simulation also shows a shear plane extending up through the dense Monterey sand berm just upstream of the soil-cement treatment zone, along with complementary shear planes dipping down to the left in the embankment against the left side of the container (Fig. 19). These shear bands indicate a rotational mechanism of embankment deformation that would increase crest settlement without increasing horizontal berm displacements (at the location of the displacement measurements). This mechanism is also evident in the shear strain contours for the smaller PBA = 0.26 g event (Fig. 13), although the strains were much smaller. This mechanism of embankment deformation in the simulations appears more significant that observed in the experiments, which may be one factor contributing to over-prediction of crest settlements (Fig. 18).

The computed stress-strain response at the location of pore pressure transducer P1 (Fig. 2) is shown in Fig. 14b. The computed stress-strain response again shows the loss of soil stiffness in the first couple of cycles as pore pressures rose rapidly, followed by a progressive accumulation of shear strains with each cycle of loading. The shear strains in this event accumulate a bit more than twice as rapidly as during the PBA = 0.26 g event (Fig. 14a), which was expected given the stronger shaking intensity. For both events, the shear stress acting on the soil element at the end of shaking is smaller than at the start of shaking because shear stresses have been redistributed to the surrounding stiffer zones (i.e. the embankment and soil-cement wall zone). The computed responses and their differences in the two events are again consistent with the behaviors expected based on single-element simulations performed during the constitutive model calibration process (e.g. Figs. 6 and 7, and Ziotopoulou and Boulanger [26]).
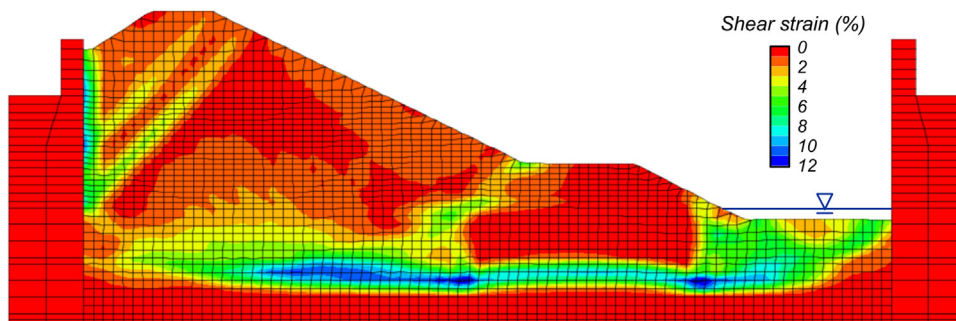
Fig. 13. Contours of shear strain after shaking for the simulation of the Kobe 0.26 g event.
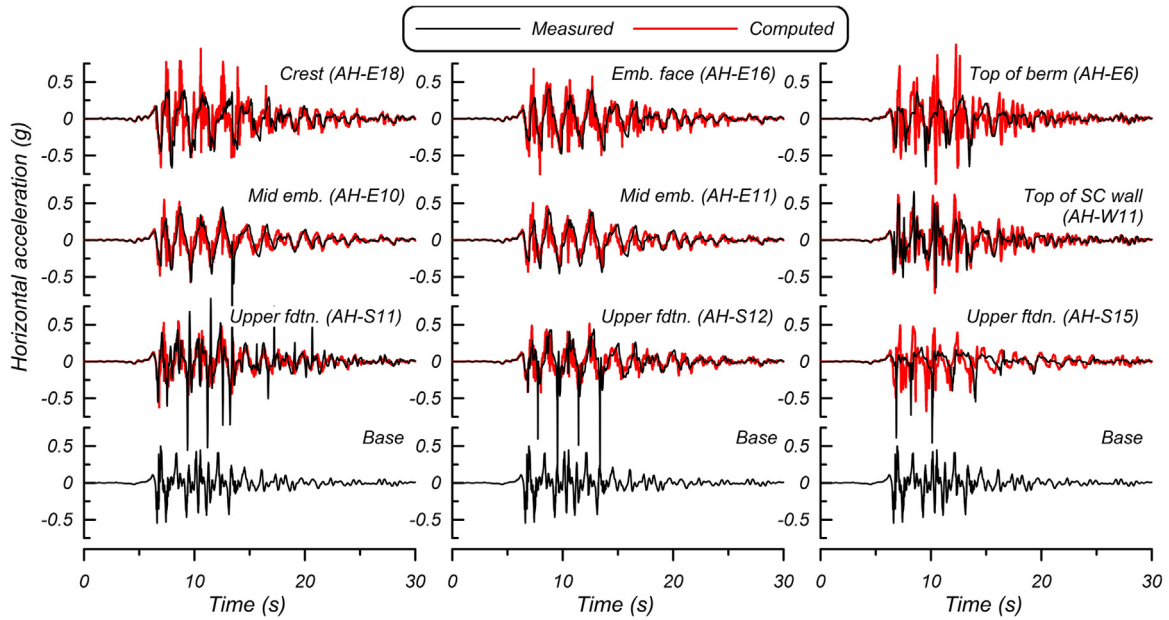
Fig. 15. Measured and computed accelerations for the Kobe 0.54 g event.

5.3. Parametric analyses

The effect of soil-cement strength on the computed crest settlements and berm horizontal displacements are shown in Fig. 20(a) and (b), respectively, for both the PBA = 0.26 and 0.54 g events. Analyses were repeated with soil-cement strengths of 0.6, 0.8, 1.0, and 1.5 times $q_{ucs}/2$. The horizontal berm displacement was more sensitive to the soil-cement strength for both shaking events, with the horizontal displacements for a strength of 0.6 $q_{ucs}/2$ being 4–6 times greater than for a strength of $1.5q_{ucs}/2$. The vertical crest settlement was much less sensitive to this range of soil-cement strengths for either shaking event, with crest settlements for a strength of 0.6 $q_{ucs}/2$ being only 25–40% greater than for a strength of $1.5q_{ucs}/2$. The lower sensitivity of crest settlement to soil-cement shear strength is attributed to the fact that crest slumping due to horizontal movements or rotations in the embankment can be associated with (1) horizontal displacement of the treatment zone and overlying berm, or (2) the shear mechanism that passes over the treatment zone, as seen in Figs. 13 and 19. The analysis results indicate that increasing the strength of the treatment zone, for the range of strengths examined, did not significantly reduce embankment displacements, but rather caused more of the movements to be associated with the shear zone passing above the treatment zone. However, further reductions in the strength of the treatment zone eventually leads to much larger crest settlements, as illustrated by the analyses for the non-treated case presented later.

The effect of tensile yielding in the soil-cement was evaluated using several different modeling alternatives for representing the effect that tensile yielding has on pore pressures within the treatment zone. The tensile strength for the soil-cement was set to $0.1q_{ucs}$ (i.e., 0.2 MPa), which gives an equivalent composite tensile strength of 0.05 MPa. One set of analyses included the above tensile strength with no other parameter changes. In these analyses, tensile yielding of the treatment zone generated negative pore
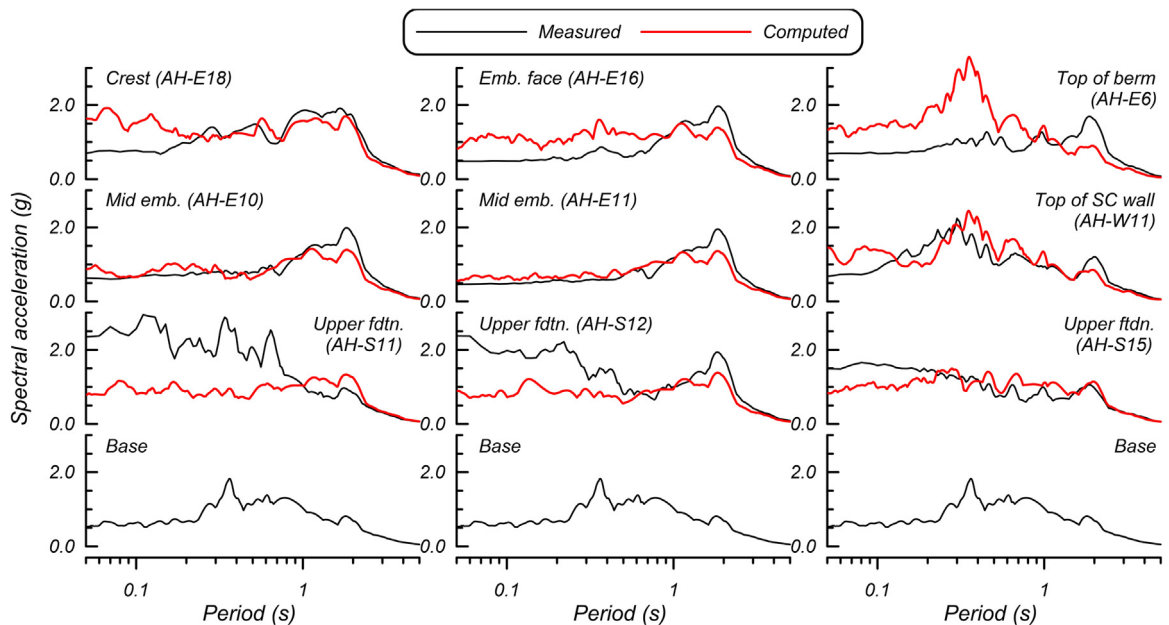
Fig. 16. Measured and computed accelerations for the Kobe 0.54 g event.
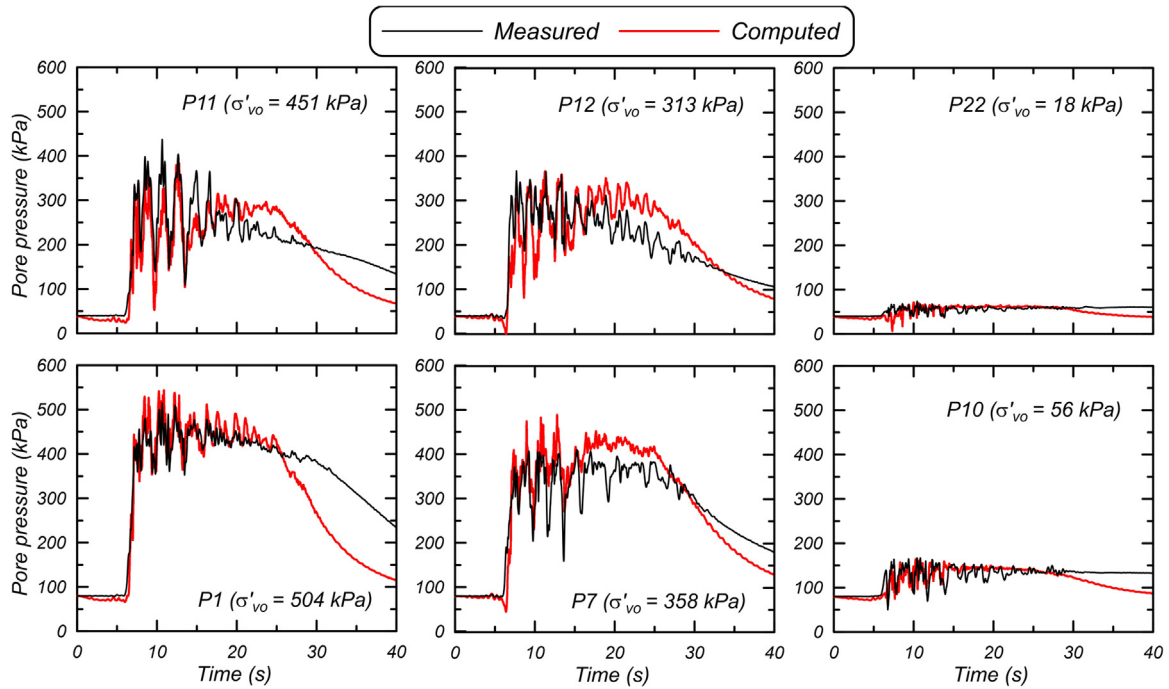
Fig. 17. Measured and computed excess pore water pressures for the Kobe 0.54 g event.
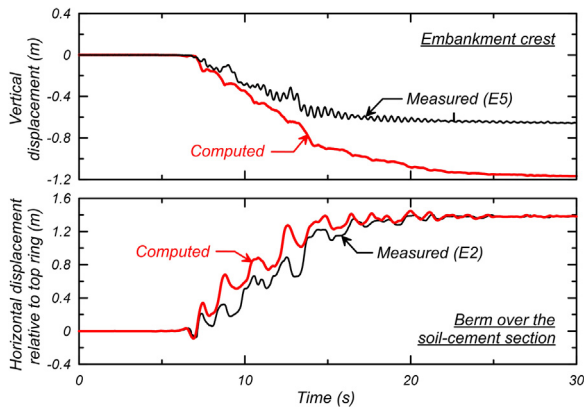
Fig. 18. Measured and computed crest settlement and berm horizontal displacement for the Kobe 0.54 g event.

water pressure increments, which increased effective stresses and reduced the potential for tensile yielding in subsequent dynamic loading cycles. In addition, the decreased pore pressures in the treatment zone increased the inflow of pore water from adjacent sand zones, which increased the strength of sand zones immediately adjacent to the treatment zone. The net effect was a 0–8% reduction in crest and berm displacements for the two shaking events. A second set of analyses was performed with the tensile strength of the water set to zero in the treatment zone, such that the pore pressures could not go negative during tensile yielding; the net effect was similar to the previous case, with a 2–7% reduction in crest and berm displacements for both shaking events. A third set of analyses was performed with the tensile strength of the water in the treatment zone set to zero and the hydraulic conductivity of the treatment zone reduced by a factor of 100 to reduce the inflow of pore water to the treatment zone. In these analyses, the crest and berm displacements increased by 1–9% for both shaking events (relative to the baseline case without tensile yielding). The results of these sensitivity analyses showed the effect of incorporating tensile yielding depends on how the pore fluid is modeled, and that the effects were relatively small for the various modeling procedures examined. However, these analyses, with the treatment zone modeled as a Mohr Coulomb material, do not account for the effects of progressive damage or cracking associated with tensile yielding.

The effect of the Ottawa sand's cyclic strength was evaluated by repeating the analyses for both shaking events with the model calibrations for a cyclic resistance ratio, for 3% shear strain in 15 uniform loading cycles at σ'_{vc} = 400 kPa, of 0.093 and 0.120. Analyses using the larger cyclic resistance ratio, compared to the smaller cyclic resistance ratio, gave 37% less crest settlement and 24% less berm displacement for the PBA = 0.26 g event and 24% less crest settlement and 13% less berm displacement for the PBA = 0.54 g event.
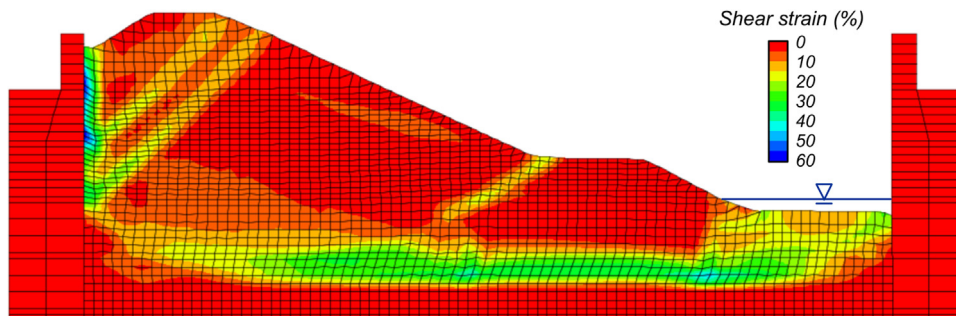
Fig. 19. Contours of shear strain after shaking for the simulation of the Kobe 0.54 g event.
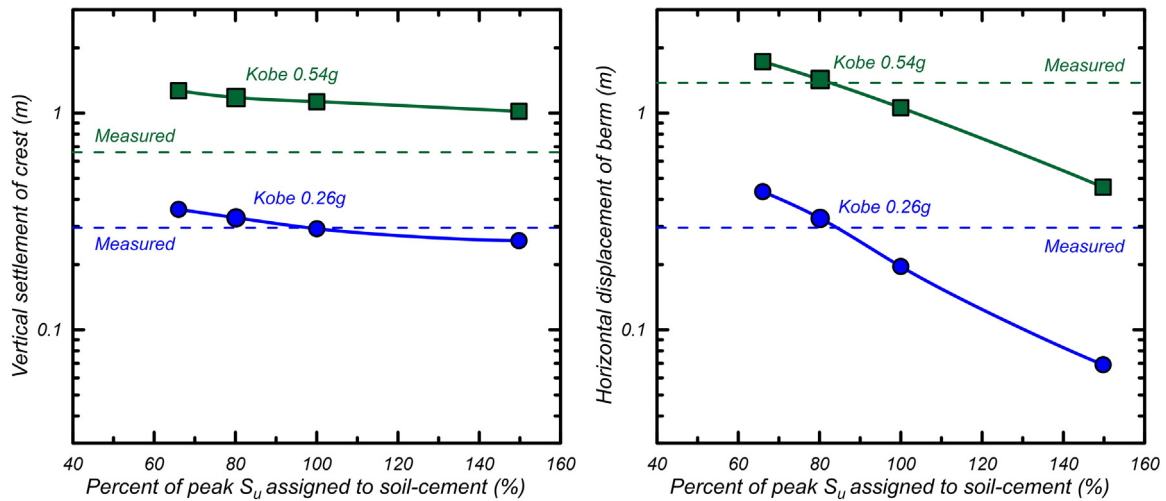
Fig. 20. Effect of soil-cement shear strength on crest settlement and berm displacement for both events.

The effect of loading history was evaluated by repeating an analysis for the PBA = 0.54 g event using the deformed model from the prior PBA = 0.26 g event, without any re-initialization of stresses or internal variables. The crest settlement increase 29% for this case, with the increase attributed to loosening (dilation) along the shear localizations that had formed in the dense Monterey embankment during the PBA = 0.26 g event (Fig. 13). The loosening of the sand along these shear zones reduced the embankment's resistance to deformations during the subsequent stronger shaking event.

The effect of the container stiffness was evaluated by repeating an analysis for the PBA = 0.26 g event with the shear modulus of the rubber layers increased or decreased by a factor of 2. Increasing the container stiffness reduced the crest settlement by < 1% but reduced the berm displacement by 10%. Reducing the container stiffness increased the crest settlement by 10% and increased the berm displacement by 8%.

5.4. Non-treated embankment

Simulations were repeated with the treatment zone omitted from the numerical model to provide a basis for evaluating the effectiveness of the soil-cement walls in reducing deformations. The deformed shape with contours of shear strain for the non-treated embankment subjected to the PBA = 0.54 g event is shown in Fig. 21. The crest settled 3.1 m (about 4.7 times the measured value) and the berm displaced horizontally 5.0 m (about 3.6 times the measured value). These results illustrate that the soil-cement walls were effective in substantially reducing deformations relative to those that would be expected in the absence of the foundation improvement.

6. Discussion

The numerical approximation of the treatment zone as a Mohr Coulomb material with equivalent composite properties does not account for a number of complex interaction mechanisms. Post-test excavation of the centrifuge model (Fig. 3) showed that deformation of the treatment zone included a component of the enclosed liquefied sand displacing relative to the soil-cement walls (i.e. extruding between the walls). The significance of this extrusion mode to the overall deformations varied across the width of the container and appeared to vary along the length of the walls (e.g., local slumping of the overlying berm at the downstream toe would be expected to increase the role of extrusion near the downstream end of the walls). The post-test inspections of soil-cement walls showed irregular cracking and offsets that varied along the length of the walls and between adjacent walls (Fig. 4). The development of offsets along these undulating crack surfaces was likely accompanied by local fluctuations in normal stress. Those changes in normal stress would contribute to changes in excess pore pressure, beyond those due to shearing alone. The net average excess pore pressures in the soil-cement during shearing would be expected to be negative based on typical undrained shearing responses of soil-cement specimens, the measured strength of the soil-cement for this model test, and the range of overburden stresses acting in this model test (e.g. Tatsuoka and Kobayashi [21]). Excess pore pressures in the enclosed liquefied sand would be expected to diffuse into the cracks in the soil-cement walls during strong shaking, which would be expected to reduce the mobilized shear resistance in the walls. The rate of pore pressure diffusion from the liquefied sand into these cracks would depend on the soil's hydraulic conductivity, the aperture of the wall cracks, the wall thickness, and the difference in pore pressures between the soil and wall materials. In addition, the shear resistance provided by
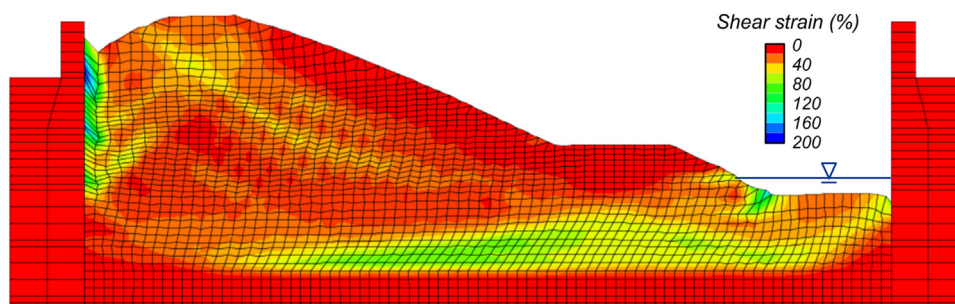
Fig. 21. Contours of shear strain after shaking with the Kobe 0.54 g event for the model without any soil-cement treatment zone (i.e. the non-treated case).

the walls would be expected to degrade progressively during shaking as the cracks grow and develop offsets.

The seismic performance of soil-cement walls in the field may also be affected by details not represented in the centrifuge or numerical models. The configuration of soil-cement walls in the field often includes longitudinal connecting walls to form a grid, or a set of grid cells with intermittent spaces between them to avoid fully impeding ground water flow. The presence of longitudinal walls should reduce the extrusion of liquefied soils between the transverse walls, which would be expected to help reduce potential ground displacements. Vertical joints in soil-cement walls constructed as overlapping columns have a smaller area ratio compared to the average area ratio for horizontal planes. Yielding along these vertical joints due to their lower area ratio or possibly lower shear strengths would be expected to reduce the lateral stiffness and strength of the wall system. Estimates of soil-cement shear strength for the field requires accounting for increases with age (a beneficial effect), spatial variability (a potential detrimental effect if not appropriately accounted for), and curvature of the strength envelope at lower confining stresses (e.g., Filz et al. [8]). Guidance for addressing these and other details important to the design of soil-cement support systems is provided in Kitazume and Terashi [15] and Bruce et al. [7].

The mechanisms affecting performance of soil-cement wall systems during strong shaking are too complex to simulate directly in most practical applications, and hence it is common to use simpler equivalent composite system models with conservative selections for the input parameters/strengths. The good agreement obtained between 2D numerical simulations and measured centrifuge model responses in the present study suggest that equivalent composite system models may be a reasonable approximation for the type of embankment system examined in this centrifuge model study. Nonetheless, there is a need for continued development and validation of numerical simulation procedures for soil-cement wall systems, which would benefit from further physical model testing and improved instrumentation at treated sites (e.g., inclinometer casings in the soil-cement walls, between the walls, and outside the treatment areas) to enable gathering key data in future earthquakes.

7. Conclusion

Two-dimensional nonlinear dynamic analyses were presented for a centrifuge model of an embankment dam on a liquefiable foundation layer treated with soil-cement walls. The centrifuge model corresponded to a 28 m tall embankment underlain by a 9 m thick saturated loose sand layer. Soil-cement walls were constructed through the loose sand layer over a 30 m long section near the toe of the embankment with a replacement ratio of 24%. The model was shaken with scaled earthquake motions having peak horizontal base accelerations of 0.05 g, 0.26 g, and 0.54 g. The numerical solutions were performed using the finite difference program FLAC [11] with the user-defined constitutive model PM4Sand (Boulanger and Ziotopoulou [6]) for the foundation and embankment sands. The soil-cement treatment zone was represented in the 2D analyses as a Mohr-Coulomb material with composite, area-weighted properties. The average shear strength of the soil-cement during shaking was taken as 80% of its peak undrained shear strength, which in turn was taken as one-half its unconfined compressive strength.

The results of the numerical simulations were in reasonable agreement with the recorded dynamic responses, including the triggering of liquefaction in the loose sand layer during the PBA = 0.26 g and 0.54 g events. The simulations reasonably approximated the observed deformation magnitudes and patterns, and correctly predicted that the soil-cement walls would shear through their full length in the largest

shaking event. Parametric analyses illustrated the effects of varying the shear strength of the soil-cement, the procedures for modeling tensile yielding of the soil-cement, the cyclic strength of the loose sand layer, and the dynamic loading history. The results of these comparisons provide support for the use of these numerical modeling procedures, including the representation of a treatment zone with area-weighted composite properties, for analyses of embankment dams with soil-cement treatment of liquefiable soils in their foundations.

References

[1] Armstrong RJ, Boulanger RW. Numerical simulations of liquefaction effects on piled bridge abutments. In: Proceedings of the 6th international conference on earthquake geotechnical engineering, Christchurch, New Zealand; 2015.

[2] Barron R.F., Kramer C., Herlache W.A., Wright J., Fung H., Liu C., 2006. Cement deep soil mixing remediation of Sunset North Basin Dam. Dam Safety 2006, ASDSO.

[3] Bolton MD. The strength and dilatancy of sands. Géotechnique 1986;36(1):65–78.

[4] Boulanger RW, Khosravi M, Khosravi A, Wilson DW. Remediation of liquefaction effects for an embankment using soil-cement walls: Centrifuge and numerical modeling. Performance-based Design in Earthquake GeotechnicalEngineering, PBD-III Vancouver, M., Taiebat et al., eds., ISSMGE Technical Committee TC203, paper 537; 2017.

[5] Boulanger RW, Ziotopoulou K. Formulation of a sand plasticity plane-strain model for earthquake engineering applications. J. Soil Dyn. Earthq. Eng. 2013;53:254–67. https://doi.org/10.1016/j.soildyn.2013.07.006.

[6] Boulanger RW, Ziotopoulou K. PM4Sand (Version 3): A sand plasticity model for earthquake engineering applications. Report No. UCD/CGM-15/01, Center for Geotechnical Modeling, UC Davis, CA; 2015.

[7] Bruce ME, Berg RR, Filz GM, Collin JG, Terashi T, Yang DS. FHWA design manual: deep mixing for embankment and foundation support. FHWA-HRT-13-04. Washington DC: Federal Highway Administration; 2013. [244 p].

[8] Filz G, Reeb A, Grenoble A, Abedzadeh F. Material Properties for Analysis of Deep Mixing Support Systems. In: Proceedings of the deep mixing 2015 Conference. Hawthorne, NJ: Deep Foundations Institute; 2015. p. 823–34.

[9] Friesen S, Balakrishnan A. General approach used for the seismic remediation of Perris Dam. In: Proceedings of the 32nd annual USSD conference, United States Society on Dams; 2012.

[10] Fukutake K, Ohtsuki A. Three dimensional Liquefaction analysis of partially improved ground. In: Proceedings of the first international conference on earthquake geotechnical engineering. Japan; 1995. p. 863-868.

[11] Itasca. FLAC, Fast Lagrangian Analysis of Continua, User's Guide, Version 8.0. Minneapolis, MN: Itasca Consulting Group, Inc; 2016.

[12] Khosravi A, Khosravi M, Yunlong W, Pulido A, Wilson DW, Boulanger RW. Remediation of liquefaction effects for a dam using soil-cement walls: data Report 1: test AKH01. Davis, CA: University of California; 2016.

[13] Khosravi A, Khosravi, Boulanger RW, Wilson DW, Pulido A. Dynamic centrifuge test of an embankment on liquefiable soil reinforced with soil-cement walls. Performance-based Design in Earthquake Geotechnical Engineering, PBD-III, Vancouver, July 16-19; 2017.

[14] Kirby RC, Roussel GL, Barneich JA, Yiadom AB, Todaro SM. Design and construction of seismic upgrades at San Pablo Dam using CDSM. Proceedings of the 30th Annual USSD Conference, United States Society on Dams; 2010. p. 137–151.

[15] Kitazume M, Terashi M. The Deep Mixing Method. Leiden, The Netherlands: CRC Press/Balkema; 2013.

[16] Namikawa T, Koseki J, Suzuki Y. Finite element analysis of lattice-shaped ground improvement by cement-mixing for liquefaction mitigation. Soils Found 2007;47(3):559–76.

[17] Parra Bastidas AM. Ottawa F-65 sand characterization [Doctoral dissertation]. Davis, CA: University of California at Davis; 2016.

[18] Parra Bastidas, A.M., Boulanger, R.W., Carey, T.J., DeJong, J.T. Ottawa F-65 Sand Data from Ana Maria Parra Bastidas, NEEShub; 2016. ⟨http://dx.doi.org/10.17603/DS2MW2R⟩.

[19] Parra Bastidas AM, Boulanger RW, DeJong JT, Price AB. Effects of pre-strain history on the cyclic resistance of Ottawa sand. Proceedings of the 16th World Conference on Earthquake Engineering, 16WCEE, paper 1213; 2017.

[20] Tamura S, Khosravi M, Wilson DW, Rayamajhi D, Boulanger RW, Olgun CG, Wang Y. Simple method for detecting cracks in soil-cement reinforcing elements for geotechnical centrifuge tests. Int J Phys Model Geotech 2018. https://doi.org/10.1680/jphmg.17.00036.

[21] Tatsuoka F, Kobayashi A. Triaxial strength characteristics of cement-treated soft clay. In:

Proceedings of the 8th European Conference of SMFE, Helsinki, Finland; 1983. p. 421–26,.

[22] Wilson DW, Boulanger RW, Kutter BL, Abghari A. Aspects of dynamic centrifuge testing of soil-pile-superstructure interaction. In: Nogami T, editor. Observation and modeling in numerical analysis and model tests in dynamic soil-structure interaction problems. ASCE; 1997. p. 47–63. [Geotechnical Special Publication No. 64].

[23] Wooten L, Foreman B. Deep soil mixing for seismic remediation of the Clemson upper and lower diversion dams. In: Proceedings of the 25th annual USSD conference, United States Society on Dams; 2005.

[24] Zhang F, Fredlund DG. Examination of the estimation of relative permeability for unsaturated soils. Can Geotech J 2015;52:2077–87.

[25] Ziotopoulou K, Boulanger RW. Calibration and implementation of a sand plasticity plane-strain model for earthquake engineering applications. J Soil Dyn Earthq Eng 2013;53:268–80. https://doi.org/10.1016/j.soildyn.2013.07.009.

[26] Ziotopoulou K, Boulanger RW. Plasticity modeling of liquefaction effects under sloping ground and irregular cyclic loading conditions. J Soil Dyn Earthq Eng 2016;84:269–83. https://doi.org/10.1016/j.soildyn.2016.02.013.